doi:10.1038/nature11882

	Model	σ{T} (K)	σ{dCO$_2$/dt} (ppmv/yr)	Corr. Coeff. r	IAV Sensitivity (ppmv/yr/K)
A	HadCM3LC	0.17	1.85	0.88	9.7 +/- 0.7
B	IPSL	0.07	1.16	0.50	8.2 +/- 2.1
C	MPI	0.21	1.59	0.75	5.7 +/- 0.7
D	CCSM1	0.07	0.57	0.53	4.5 +/- 1.0
E	FRCGC	0.14	0.97	0.81	5.8 +/- 0.6
F	LOOP	0.15	1.61	0.28	2.9 +/- 1.4
G	HadCM3C-st	0.16	2.33	0.88	12.5 +/- 1.1
H	HadCM3C-a	0.15	1.14	0.72	5.6 +/- 0.8
I	HadCM3C-h	0.17	3.61	0.70	14.4 +/-2.3
	Obs (NCDC)	0.09	0.75	0.65	5.1 +/-0.9
	Obs (with Volc)	0.09	0.83	0.58	5.3 +/-1.1
	Obs (HadCRU3)	0.10	0.75	0.64	4.6 +/-0.8
	Obs (GISS)	0.10	0.75	0.66	4.9 +/-0.9
	Obs (RCP CO$_2$)	0.10	0.52	0.73	3.8+/-0.6
	Obs (GMD CO$_2$)	0.09	0.85	0.67	6.7+/-1.5

Table S1: Sensitivity of the annual growth-rate of CO_2 to tropical temperature variability. Statistical measures of the variability in the annual mean tropical temperature (**T**) and annual growth-rate of atmospheric CO_2 (**dCO$_2$/dt**), for each of the climate-carbon cycle models used in this study (**A – I**) and various combinations of observational datasets (the NCDC, HadCRU3 and GISS observational datasets to calculate annual tropical temperature anomalies, and the RCP and GMD datasets for global CO_2). These parameters are typically calculated over the period 1960-2010 inclusive, except for the RCP and GMD estimates which are calculated over the sub-period covered by these datasets, 1960-2004 and 1980-2010 respectively. In all but one case, the post volcano years (1963, 1964, 1982, 1983, 1992, 1993) are excluded from the observational time-series. The exception to this is the row labelled "Obs (with Volc)" which is calculated using the NCDC climate data, but with these post-volcano years included. Unless otherwise stated the observational estimates use the global CO_2 record constructed by concatenating the RCP CO_2 data for 1960-1979 with the GMD CO_2 data for 1980-2010, and the NCDC tropical temperature anomalies. The second and third columns show the standard deviation (**σ**) of the tropical temperature and the CO_2 growth-rate respectively; the fourth column shows the correlation coefficient (**r**) between these variables; and the fifth-column shows the best-fit gradient for the least squares linear regression between dCO_2/dt and T, with the uncertainty representing plus and minus one standard error. The latter sensitivity coefficient is equal to **r. σ{dCO$_2$/dt}/σ{T}.** In all but one case the linear regressions have $p<0.001$, and in the remaining case (model F) $p<0.05$.

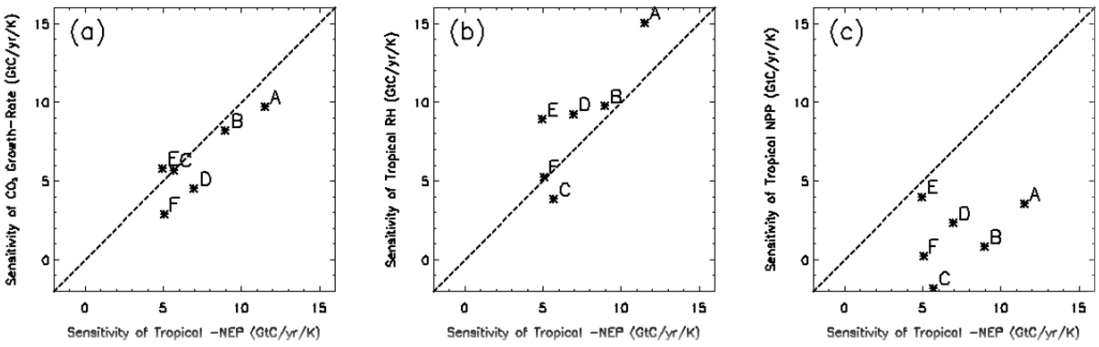

Figure S1: Contribution of tropical land-atmosphere fluxes to the sensitivity of the annual CO_2 growth-rate to tropical temperature variability. Scatter plots across the C^{4}MIP models, showing the relationship of the interannual sensitivity of the tropical Net Ecosystem Productivity (NEP) to the interannual sensitivity of (a) the CO_2 growth-rate ; (b) the tropical Heterotrophic (or soil) Respiration (RH); and (c) the tropical Net Primary Productivity (NPP). Panel (a) shows that variations in the sensitivity of the CO_2 growth-rate are largely due to variations in the sensitivity of the tropical NEP. Panels (b) and (c) demonstrate that the large range of sensitivity of NEP is mainly due to the differing sensitivities of soil respiration rather than net primary productivity.

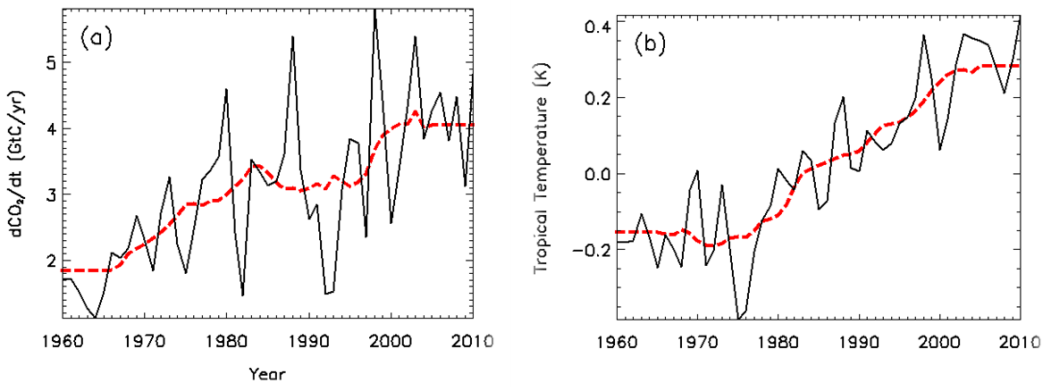

Figure S2: Observational data for (a) the growth-rate of atmospheric CO_2[26,27]and (b) the tropical mean temperature anomaly[28]. In each case the continuous black line shows the annual mean value and the red dotted-line shows the 11-year running mean. The difference between these defines the annual anomalies used to derive the observational constraint on the IAV Sensitivity, as shown in Figure 2.

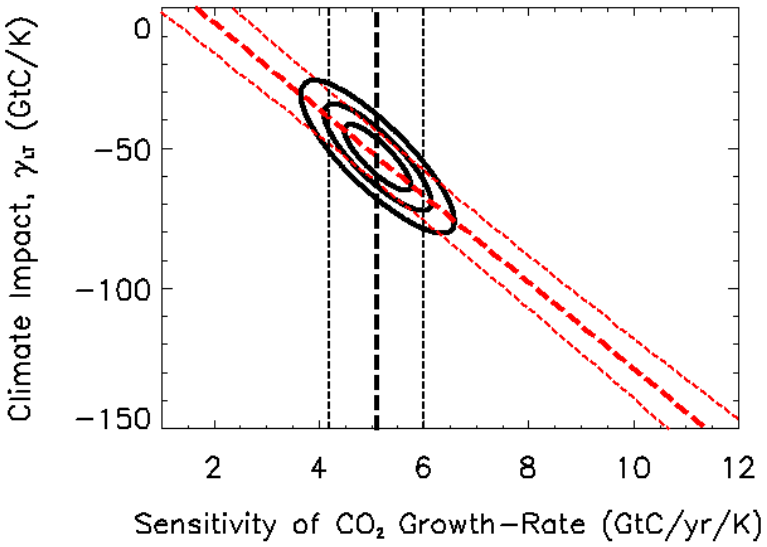

Figure S3: Contours of probability density for the linear regression shown in Figure 3a. The thick red dashed-line shows the best-fit linear regression, and the thin red lines show plus and minus the σ_f prediction error (see Methods). The vertical black lines show the observational constraint on the IAV Sensitivity, with the best fit shown by the thick dashed black line, and the thin vertical dashed lines showing plus and minus one standard error about this value. The continuous black contours are the product of these two underlying PDFs. The integral of these contours across the x-axis variable leads to the IAV-constrained PDF shown in Figure 3b.